Original Article

Numerical modeling of bed deposition in rapid flow-like landslides: a case study of the Gaolou landslide in Shaanxi Province, China

SHEN Wei[1] https://orcid.org/0000-0001-9427-5029; e-mail: shenweichd@qq.com

LI Tong-lu[2]* https://orcid.org/0000-0001-6561-1871; ✉ e-mail: dcdgx08@chd.edu.cn

BERTI Matteo[1] https://orcid.org/0000-0003-1588-2002; e-mail: matteo.berti@unibo.it

LI Ping[2]* https://orcid.org/0000-0002-6010-961X; ✉ e-mail: dcdgx07@chd.edu.cn

LEI Yu-lu[2] https://orcid.org/0000-0002-2931-6696; e-mail: 540762906@qq.com

SHEN Yue-qiang[2] https://orcid.org/0000-0001-6659-6327; e-mail: 825177498@qq.com

*Corresponding author

1 Department of Biological, Geological and Environmental Sciences, University of Bologna, Bologna 40126, Italy

2 Department of Geological Engineering, Chang'an University, Xi'an 710064, China

Abstract: Some flow-like landslides tend to lose materials while moving on a relatively dry sliding surface. This phenomenon is called bed deposition. In contrast to the bed entrainment phenomenon, bed deposition is relatively poorly understood. Therefore, an improved depth-averaged model is proposed to quantify this phenomenon. The deposition depth is calculated according to the momentum conservation of the deposited mass, and the rheological property of the sliding mass on the bottom is modified considering an abrupt increase in the depth of the sliding surface after deposition. Utilizing the proposed model, the Gaolou landslide, a typical flow-like landside occurring on October 6th, 2006 with an obvious bed deposition phenomenon in Shaanxi Province of China, is simulated to investigate the influence of bed deposition on its propagation process. The results indicate that the proposed model can effectively depict the bed deposition phenomenon in the Gaolou landslide. Bed deposition dissipates part of the kinetic energy of this landslide; thus, the simulated debris inundation area would likely be overestimated when this effect is neglected. On the other hand, the thin liquefied layer formed by the bed deposition process reduces the friction energy dissipation, contributing to the high mobility of this landslide.

Keywords: Natural hazards; Flow like landslides; Numerical simulation; Depth-averaged model; Bed deposition

1 Introduction

Among the mass movements occurring in mountainous areas, rapid flow-like landslides may be the most dangerous owing to their hypermobility and destructive potential in the debris inundation area. Debris flows, debris avalanches, mudflows, and lahars

are typical rapid flow-like movements (Hungr et al. 2014) that frequently pose threats to public security. As a consequence of some of these catastrophic events, thousands of people were dead and billions of dollars were spent in the past few decades (Evans et al. 2009, Haque et al. 2016, Huang et al. 2012, Pierson et al. 1990, Tsou et al. 2011). Therefore, it is of considerable importance to understand the mechanism of these landslides and to predict the propagation processes of potential events in the future.

One major question closely related to these landslides, which is of great interest to geoscientists, is why these landslides show hypermobility (i.e., normally the ratio of drop height to runout distance is smaller than 0.6). Different hypotheses have been proposed to explain the mechanism of this hypermobility, such as excess pore (water/gas) pressure (Alonso et al. 2016, Chen et al. 2015, Goren and Aharonov 2007, Okada et al. 2005, Sassa et al. 2014, Wang et al. 2013), self-lubrication of the sliding mass (Campbell 1989, Wang et al. 2017), and release of elastic energy due to landslide disintegration (Davies and McSaveney 2009, Perinotto et al. 2015). Presently, the excess pore pressure hypothesis may be the most commonly accepted model not only because it is easy to validate, but also because it can explain some phenomena associated with rapid flow-like landslides, such as the bed entrainment-induced hypermobility (Hungr and Evans 2004, Iverson 2012, Iverson and Ouyang 2015, Mangeney 2011, Mergili et al. 2018, Shen et al. 2019b).

Excess pore pressure may also play an important role in bed deposition. Bed deposition is the opposite process of bed entrainment in terms of mechanical processes (Pudasaini and Fischer 2016). In contrast to bed entrainment, bed deposition reduces the total volume of a landslide, while simultaneously maintaining the high mobility of the landslide. This phenomenon can be easily explained through the excess pore pressure theory. Because bed deposition usually occurs when the bed is relatively dry and the sliding mass on the bottom is saturated, a thin layer of saturated mass will form after deposition. In this thin layer of saturated mass, excess pore water pressure is likely to be generated given the rapid shear forces exerted by the sliding mass.

Numerical simulation can help estimate and analyze the propagation processes of these flow-like landslides. Techniques in this field have developed rapidly in recent years, with an increasingly large number of models being put forward (Crosta et al. 2009, Liu and Huang 2006, Liu et al. 2019, McDougall and Hungr 2005, Medina et al. 2008, Ouyang et al. 2013, Ouyang et al. 2017, Pastor et al. 2009, Pirulli and Pastor 2012, Pudasaini 2012, Sassa et al. 2014, Shen et al. 2019a, Shen et al. 2018). Most of these existing models, however, mainly focus on bed entrainment. This is because bed entrainment is easier to measure than bed deposition in the field, and entrainment is an important process that controls the rate of volume increase during the flow. Several studies in the literature (Cuomo et al. 2016, Kang and Chan 2018, Kang et al. 2017, Mergili et al. 2018) have documented the process of bed entrainment and its impact on the propagation processes of flow-like landslides. On the other hand, although a few models (Liu and He 2020) have taken bed deposition into account by using some empirical formulations, the mechanics of bed deposition and its impact on the runout process of flow-like landslides are still relatively poorly understood.

In this study, we propose an improved numerical model to quantify the bed deposition phenomenon in rapid flow-like landslides. In the next section, the principle of the model is introduced and incorporated into a quasi-three-dimensional finite difference model (Shen et al. 2018). Then, the numerical model is validated by simulating a debris flow flume experiment, and the influence of bed deposition on the runout process of a typical flow-like landslide is analyzed using our conceptual model. Finally, the results of several parametric studies using our new numerical model are presented and discussed before drawing the conclusions.

2 Basic Principles of the Bed Deposition Model

2.1 Governing equations

When a flow-like landslide travels on a relatively dry bed, part of the sliding mass will deposit on the bed if the bottom of the sliding mass is saturated. As a result, a thin layer of deposited mass will form. Assuming that there is no entrainment along the path, the total volume of the final deposit will be smaller than the original volume of the landslide. This bed deposition process is schematically shown in Fig. 1.

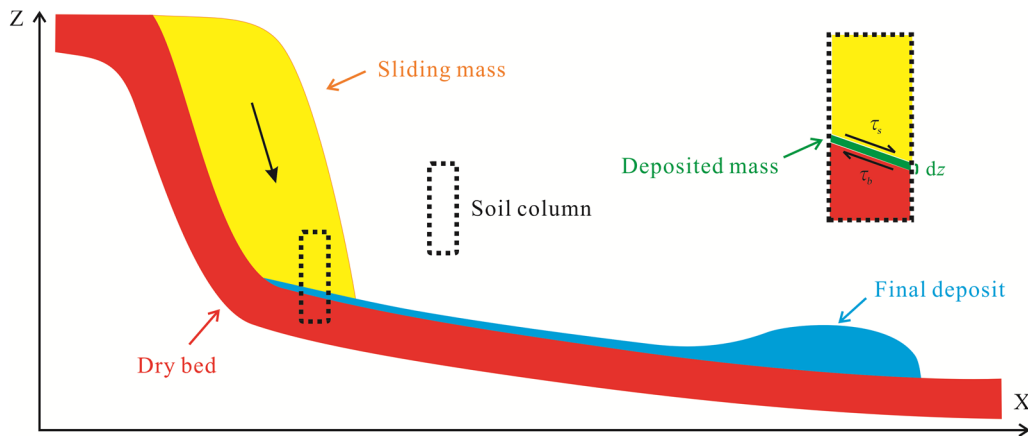The governing equations depicting the motion of

Fig. 1 Schematic diagram of bed deposition phenomenon in flow-like landslides.

a flow-like landslide usually consist of momentum and continuity equations. Considering that the scale of a flow-like landslide in the horizontal direction is usually much larger than its scale in the vertical direction, the shallow water assumption can be adopted, so that the governing equations can be simplified into depth-averaged equations. The depth-averaged governing equations used in this study are derived according to the principles of momentum and mass conservations of an arbitrary rectangular soil column (Shen et al. 2018). These equations include one continuity equation and two momentum equations, and their expressions are given by

$$\frac{\partial h}{\partial t} + \frac{\partial Q_x}{\partial x} + \frac{\partial Q_y}{\partial y} = D \tag{1}$$

$$\begin{aligned}
&\frac{\partial Q_x}{\partial t} + \frac{\partial Q_x^2 / h}{\partial x} + \frac{\partial Q_x Q_y / h}{\partial y} \\
&= -\left(k_x h g \frac{\partial h}{\partial x} + g \frac{h^2}{2} \frac{\partial k_x}{\partial x} \right) \\
&+ \left(A g + B \right) \frac{h \tan \alpha}{G} - \frac{h S_x}{m}
\end{aligned} \tag{2}$$

$$\begin{aligned}
&\frac{\partial Q_y}{\partial t} + \frac{\partial Q_x Q_y / h}{\partial x} + \frac{\partial Q_y^2 / h}{\partial y} \\
&= -\left(k_y h g \frac{\partial h}{\partial y} + g \frac{h^2}{2} \frac{\partial k_y}{\partial y} \right) \\
&+ \left(A g + B \right) \frac{h \tan \beta}{G} - \frac{h S_y}{m}
\end{aligned} \tag{3}$$

where h is the thickness of the sliding mass, Q_x and Q_y are the mass fluxes in the x and y directions, respectively, D is the deposition rate, k_x and k_y are the

lateral earth-pressure coefficients in the x and y directions, respectively, which evolve according to the state (passive, static, or active states) of the soil (Ouyang et al. 2015, Shen et al. 2018), g is the gravitational acceleration, A and B are the parameters corresponding to the static and centrifugal normal forces, respectively, α and β are the dip angles of the sliding bed in the x and y directions, respectively (i.e., $\tan\alpha = \partial Z / \partial x$, and $\tan\beta = \partial Z / \partial y$, in which Z is the bed elevation), G is a geometric parameter related to α and β, S_x and S_y are the projections of the resistance S in the x and y directions, respectively, and m is the mass of the soil column.

These equations need to be closed by adopting suitable rheological laws for the resistance S and formulations for the deposition rate D. Numerous rheological laws have been implemented in the simulation of flow-like landslides, such as the Bingham model, Voellmy model, Mohr-Coulomb model and some velocity-weakening friction laws. The applicability of each rheological law depends on the characteristics of the flow. Because the flow-like landslide here mainly consists of loess, the rheology of which can be captured well by the Mohr-Coulomb criterion, we use the Mohr-Coulomb criterion to calculate S

$$S = N(1 - r_u) \tan \varphi' + c' \Delta x \Delta y \sqrt{G} \tag{4}$$

where N is the normal force on the sliding surface, r_u is the pore pressure coefficient, which is an empirical parameter representing the ratio of the pore pressure and total stress, φ' and c' are the effective basal friction angle and cohesion, respectively, and Δx and Δy are the widths of the soil column in the x and y directions, respectively.

As for deposition rate D, there does not exist a

widely used formulation for flow-like landslides. However, some empirical models have been proposed to calculate the deposition rate for sediment transport problems in rivers (Cao et al. 2004, Chen and Zhang 2015, Croissant et al. 2017, Heyman et al. 2016). However, these models are not suitable in our case because the mechanism of bed deposition in flow-like landslides is different from fluvial sediment transport. For sediment transport, deposition occurs when the kinematic energy of the flow phase is insufficient to carry the solid particles in it. In flow-like landslides, deposition occurs when the strength of the bed material exceeds the driving shear stress. Mechanically, bed deposition in the present context is more similar to bed entrainment in flow-like landslides. A growing number of models have adopted a mechanical method to calculate bed entrainment (Ouyang et al. 2015, Pudasaini and Fischer 2016, Shen et al. 2018). This method is derived according to the principle of momentum conservation of the bed material (Fraccarollo and Capart 2002), and its expression is written as

$$E = -\frac{\partial Z}{\partial t} = \frac{\tau_s - \tau_b}{\rho_e v} \qquad (5)$$

where E is the entrainment rate, Z is the elevation of the bed, τ_s is the shear stress of the sliding mass, τ_b is the shear stress in the bed, ρ_e is the density of the entrained mass, and v is the velocity of the sliding mass. Eq. (5) indicates that the landslide will entrain mass from the bed when the driving stress of the sliding mass (τ_s) is larger than the strength of the bed material (τ_b), and at a given time, the erodible mass gains momentum with a rate of $E\rho_e v$ under the effect of an external stress $\tau_s - \tau_b$. Referring to the derivation of bed entrainment, it is possible to derive the formulation of the deposition rate in a similar way by introducing only minor changes. The formulation of the deposition rate used in this study is given by

$$D = \frac{\partial Z}{\partial t} = \frac{\tau_b - \tau_s}{\rho_s v} \qquad (6)$$

where ρ_s is the density of the sliding mass. In contrast to bed entrainment, bed deposition occurs when the strength of the bed material (τ_b) is larger than the shear stress at the bottom of the sliding mass (τ_s).

After deposition, the location of the sliding surface will shift from the bed material to the sliding mass, and so, the basal rheology should change accordingly. The following equation is proposed to

account for the sudden change in the basal rheology

$$f = \begin{cases} f_b & before \\ f_s & after \end{cases} \qquad (7)$$

where f represents any rheological parameter (i.e., r_u, φ', and c') in Eq. (4), and the subscripts b and s refer to bed material and sliding mass, respectively. Eq. (7) shows that the basal rheology parameter takes the values of the bed material and sliding mass before and after bed deposition, respectively.

By incorporating Eqs. (4), (6), and (7) into Eqs. (1-3), the modified governing equations for bed deposition are built up. They can be solved by the finite difference method (Shen et al. 2018).

2.2 Model setup and numerical scheme

In this section we briefly introduce the model setup and numerical scheme. Detailed information can be found in Shen et al. (2018).

2.2.1 Initial and boundary conditions

Because the soil columns are initially static in all control volumes, to start moving, the external forces (normal force and lateral pressure ingredient) should exceed the shear resistance. Therefore, an initial condition needs to be imposed on each static soil column. Taking the x-direction as an example (formulation in the y-direction is similar), the initial condition is given by

$$\left| -\left(k_x hg \frac{\partial h}{\partial x} + g \frac{h^2}{2} \frac{\partial k_x}{\partial x} \right) + \left(Ag + B \right) \frac{h \tan \alpha}{G} \right| > \left| \frac{h S_x}{m} \right| \quad (8)$$

There are two types of boundaries in our model when simulating a landslide. One is the free surface boundary of the landslide, which is automatically determined by the calculated thickness (h) of the landslide. Another is the wet-dry bed boundary, which separates the region occupied by the sliding mass and the dry bed. On the wet-dry bed boundary, the height and velocity of the sliding mass are zero ($v = 0$, $h = 0$). Additionally, a computational zone that is usually larger than the propagation zone of a landslide is adopted, so that no special treatments are necessary for the outside boundaries of the computational zone.

2.2.2 Numerical scheme

The governing equations above are discretized on rectangular computational cells. The thickness h is discretized at the center of these cells, and the velocity

v is discretized at the surfaces of these cells. For temporal terms (i.e., the first terms on the left-hand side of Eqs. (1-3)), the third-order Adams predictor-corrector method (Shen et al. 2018) is adopted to determine the variables at the next time step. The prediction step can be written as

$$h_{i,j}^{*t+1} = h_{i,j}^{t} + \frac{\Delta t}{12}(23H_{i,j}^{t} - 16H_{i,j}^{t-1} + 5H_{i,j}^{t-2}) + D_{i,j}^{t} \quad (9)$$

$$Q_{xi,j}^{*t+1} = Q_{xi,j}^{t} + \frac{\Delta t}{12}(23M_{i,j}^{t} - 16M_{i,j}^{t-1} + 5M_{i,j}^{t-2}) \quad (10)$$

$$Q_{yi,j}^{*t+1} = Q_{yi,j}^{t} + \frac{\Delta t}{12}(23N_{i,j}^{t} - 16N_{i,j}^{t-1} + 5N_{i,j}^{t-2}) \quad (11)$$

where the terms on the left-hand side are the predicted values of the three variables at the next time step, H is the discretized form of the spatial terms of the continuity equation, M and N are the discretized forms of the spatial terms of momentum equations in the x and y directions, respectively, i and j are the indexes for the computational cells in the x and y directions, respectively, and Δt is the time step. The correction step is given by

$$h_{i,j}^{t+1} = h_{i,j}^{t} + \frac{\Delta t}{12}(5H_{i,j}^{*t+1} + 8H_{i,j}^{t} - H_{i,j}^{t-1}) + D_{i,j}^{*t+1} \quad (12)$$

$$Q_{xi,j}^{t+1} = Q_{xi,j}^{t} + \frac{\Delta t}{12}(5M_{i,j}^{*t+1} + 8M_{i,j}^{t} - M_{i,j}^{t-1}) \quad (13)$$

$$Q_{yi,j}^{t+1} = Q_{yi,j}^{t} + \frac{\Delta t}{12}(5N_{i,j}^{*t+1} + 8N_{i,j}^{t} - N_{i,j}^{t}) \quad (14)$$

Among the spatial terms of the momentum equations, the convective terms (for example, the second and third terms on the left-hand side of Eqs. (2–3)) are discretized using the first-order upwind method. The central difference scheme is utilized to discretize all other spatial terms, which can be written as

$$\frac{\partial f}{\partial x_i} \approx \frac{f_{i+1/2,j}^{t} - f_{i-1/2,j}^{t}}{dx_i} \quad (15)$$

Using the above numerical scheme, the governing equations can be transformed into linear algebraic equations, which can be easily solved.

3 Simulation of Flume Experiment

Shen et al. (2018) performed a validation of the numerical scheme described above by simulating one ideal and one experimental case of a water dam break. To further validate the model for the simulation of bed deposition, we simulate one large flume experiment conducted by the U.S. Geological Survey (USGS) (Johnson et al. 2012). A schematic diagram of this flume experiment is illustrated in Fig. 2.

In this experiment, approximately 10 m³ of water-saturated sediment consisting of sand (0.0625-2 mm, 33%), and gravel (2-32 mm, 66%) with a trace of mud (<0.0625 mm, 1%) was released from a hopper at the head of the flume. Then, the flow propagated rapidly along a 2 m wide and 1.2 m deep channel inclined at 31° before it rushed out from the flume outlet. Finally, the flow rested on a pad inclined at approximately 2.4°. The flume walls and runout pad are smooth, while most channel lengths are roughened with small bumps, as described by Johnson et al. (2012). The flow depths at three locations in the channel, 32 m, 66 m, and 80 m
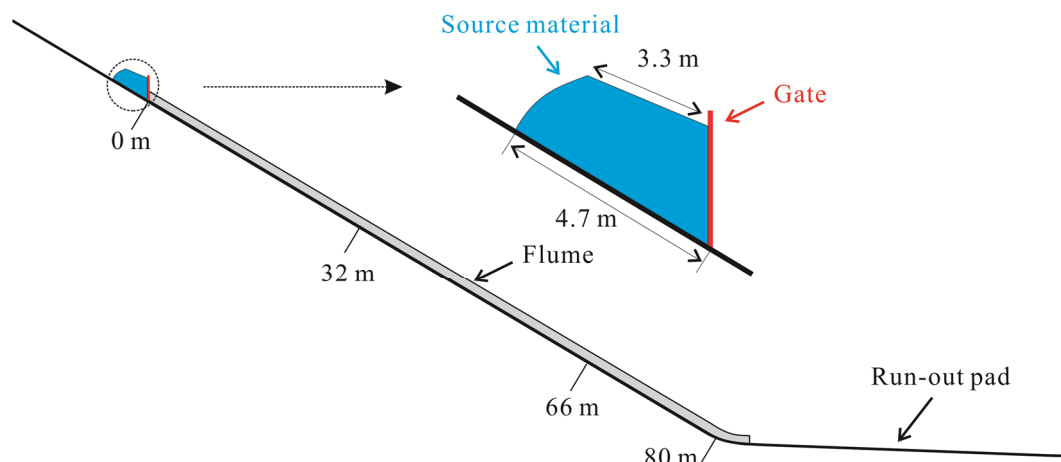

Fig. 2 Schematic diagram of the U.S. Geological Survey debris flow flume experiment. The experimental prototype is extracted from (Johnson et al. 2012).

downslope from the hopper gate, were monitored during the entire runout process of the flow. A part of the saturated flow was observed to be deposited on the channel bed, and hence we assume that bed deposition might play an important role in this experiment. Therefore, we select this case to verify the bed deposition formulation in our model. In the simulation, the effective friction angle on the bed is assumed to be approximately 30°. A small cohesion value of 0.20 kPa is assumed because the content of mud in the water-saturated mixture is very limited. The pore pressure coefficient r_u before bed deposition is assumed to be zero, while after bed deposition, the average value of r_u is assumed to be 0.30, considering the generation of excess water pressure. Uniform square computational cells are adopted in this simulation, and the size of every cell is 0.1 m. The simulation results are compared with the experimental data (Fig. 3). The results indicate that the flow characteristics at all three locations obtained by simulation agree well with the monitoring data in terms of the arrival time of the flow, maximum depth, and final deposition depth on the roughened channel bed. The main runout process of the flow ended at approximately 20 s after the discharge of the flow from the hopper. A thin layer of saturated deposit was formed on the channel bed, and the depth of the saturated deposit was approximately 0.015 m, 0.022 m, and 0.103 m at the three monitoring points 32 m, 66 m, and 80 m downslope from the hopper gate, respectively. The simulation results are in good agreement with the experimental results, indicating the good capability of our model for the simulation of bed deposition.

4   Simulation of the Gaolou Landslide

4.1 Information about the Gaolou landslide

The Gaolou landslide is a catastrophic flow-like landslide occurred in Huaxian County at the south margin of the Chinese Loess Plateau (Shaanxi Province, China). This landslide occurred on October 6th, 2006, destroyed 24 houses and caused 12 casualties (Zhang et al. 2009). Fig. 4 shows the satellite images of the landslide area before and after this event.

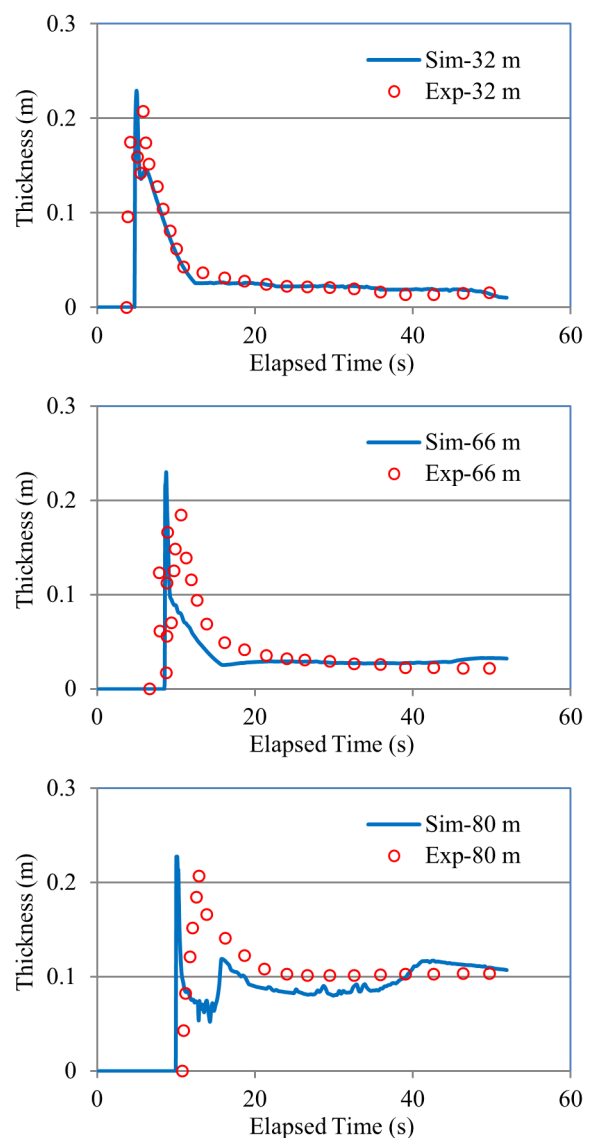From a morphological point of view, the landslide comprises a source zone, a transport zone, and a

Fig. 3 Simulation results of the flow depths at three locations downslope from the hopper gate for the U.S. Geological Survey debris flow flume experiment. The experiment data is extracted from the results of the 25th August flow in Johnson et al. (2012).

deposition zone, as shown in Fig. 5. In the first stage, approximately 25300 m³ of the loess mass detached from the slope at the top end of a small gully (Fig. 5b). Then, the failed mass turned into a rapid flow-like landslide and travelled along the meandering gully (Fig. 5a). Finally, the landslide rested in the deposition zone (Fig. 5c) where many villagers resided. Although the volume of this landslide was relatively small, it reached a long runout distance of approximately 320 m after descending 75 m in the vertical direction, inundating an area of nearly 14000 m² in its deposition zone.
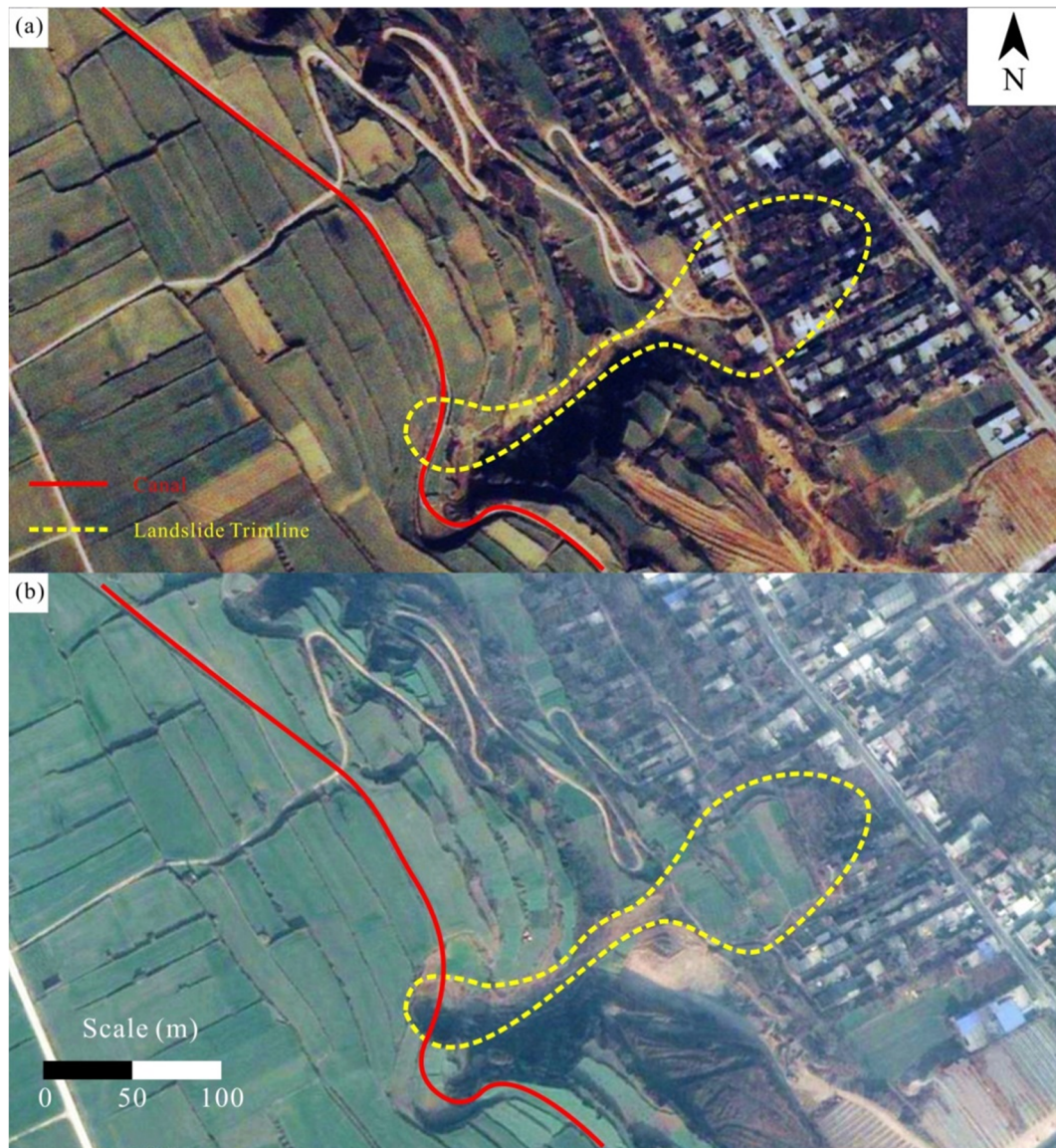
Fig. 4 Aerial view of the Gaolou landslide from Google Earth (N 34°26'20.58", E 109°39'51.34"): (a) pre-failure view on 22nd February, 2006; (b) post-failure view on 3rd January, 2015.

In the Chinese Loess Plateau, many loess landslides are directly induced by irrigation or triggered by the leakages of the irrigation canals (Li et al. 2013, Xu et al. 2012). The Gaolou landslide was triggered by the leakage of a canal (shown in Fig. 4 and Fig. 5b) on the top of the original slope. Unlike landslides triggered by heavy rainfalls, the runout path of the Gaolou landslide along the gully was relatively dry. Additionally, due to the long-term leakage of the canal, the groundwater table in the pre-failure slope increased steadily so that the loess mass near the sliding surface was already saturated before the failure. Therefore, bed deposition, rather than bed entrainment, played a dominant role in this case. A thin layer of saturated loess (i.e., the deep yellow loess along the path in Fig. 5a) was observed in the transport zone after the landslide, which indicated the existence of bed deposition in this landslide.

4.2 Simulation setup

The digital elevation model of the Gaolou landslide for this simulation is based on field survey data. The pre-failure slope and coordinate system in the simulation are shown in Fig. 6. The computational region is a rectangular area with a length of 360 m in the x direction and a width of 185 m in the y direction. The size of the computational cells is 5 m in both the x
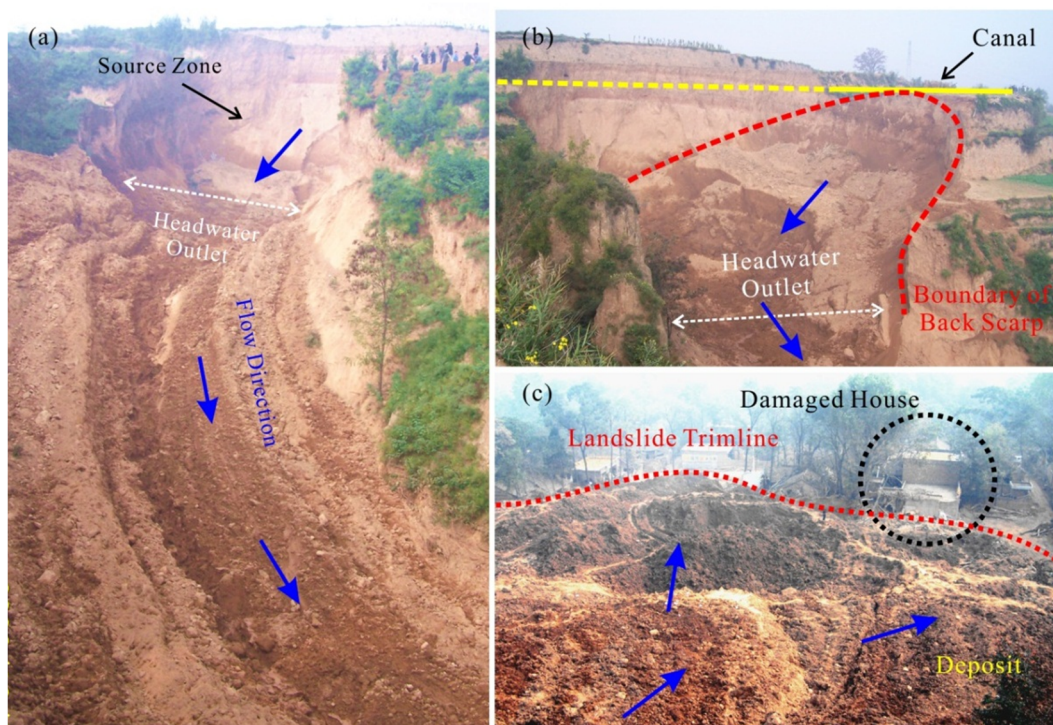
Fig. 5 Distribution zones of the Gaolou landslide: (a) transport zone (the deep yellow loess along the path is the saturated loess layer produced by bed deposition), (b) source zone and (c) deposition zone.
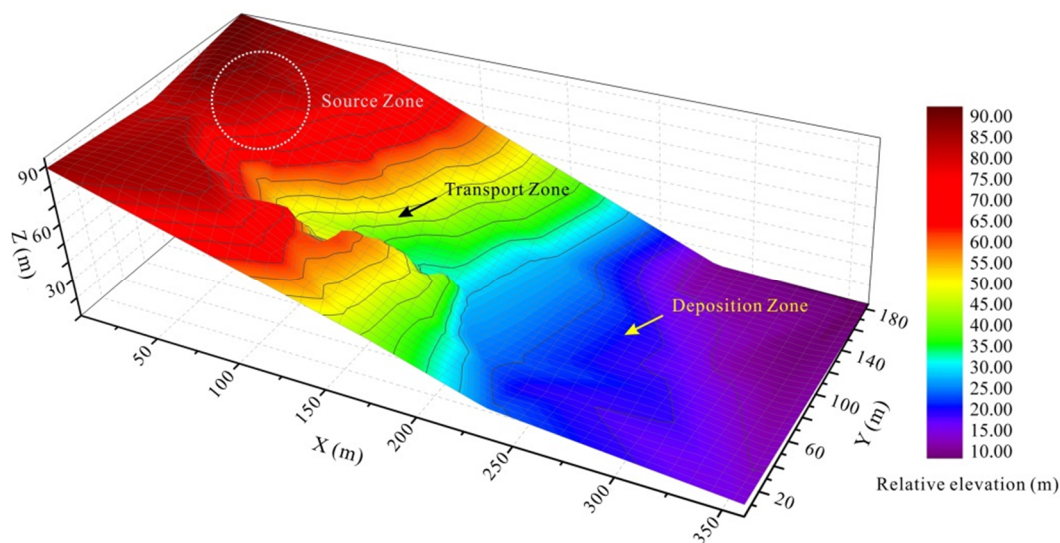

Fig. 6 Three-dimensional digital elevation model of the pre-failure topography of the Gaolou landslide.

and y directions. The initial time step is 0.005 s.

The two materials used in the simulations include dry loess for the bed material and saturated loess for the sliding mass (Table 1). The c', φ', and ρ values of the dry and saturated loess are given based on the laboratory test results from Li et al. (2013). The r_u of the bed material is assumed to be very low considering that the bed loess is dry, while that of the sliding mass has a high value given the high water

Table 1 Parameters used in simulating the Gaolou landslide which occurred in Shaanxi Province of China on October 6th, 2006

Soil type	c'	φ'	r_u	k_o	ρ
	kPa	-	-	-	g/cm³
Sliding mass	6	20.8°	0.95	0.85	1.9
Bed material	10	20.8°	0.10	-	-

Note: c' is the cohesion value; r_u is the pore pressure coefficient; φ' is the effective basal friction angle; k_o is the static lateral pressure coefficient; ρ is the loess density.

content and low permeability of the saturated loess. The k_o value of the sliding mass is estimated by $k_0 = 1 - \sin\varphi_a$, and the ρ value of the sliding mass takes the natural density of the loess in the study area. Additionally, in the deposition zone, the c' values of both the sliding mass and bed material are assumed to be 20 kPa to consider the resistance from the buildings.

Based on the parameters listed in Table 1, three different analyses are carried out to investigate the influence of bed deposition on the propagation characteristics of the Gaolou landslide. In simulation one (S1), the influence of bed deposition on the rheology and volume of the landslide is entirely neglected, and the basal rheological parameters are those of the dry bed material. In simulation two (S2), the volume reduction and rheology transition caused by the bed deposition are neglected, and the basal rheological parameters directly take those of the saturated sliding mass. In simulation three (S3), both the volume reduction and rheology transition caused by bed deposition are considered, and the basal rheological parameters are calculated based on Eq. (7).

5 Results

Fig. 7 shows the measured thickness of the landslide deposit in the deposition zone and the simulated final deposits of the three cases. The simulated runout distance and deposition area of S1 deviate significantly from the observed values (Fig. 7b). In this case, the landslide will stop moving at a very short runout distance, and it cannot transform into a rapid flow-like landslide. This result suggests that bed deposition plays a dominant role in controlling the mobility of the Gaolou landslide. The thin layer of saturated loess formed during the bed deposition process increases the pore water pressure on the bed, and thus, it reduces the frictional energy dissipation. If this influence is not considered, the simulated runout distance is likely to be greatly underestimated. In comparison, the simulated runout distance and inundated area of S2 (Fig. 7c) are already relatively close to the measured data. However, because the volume reduction caused by bed deposition is not considered in S2, the sliding mass that reaches the deposition zone may be slightly overestimated. Moreover, given that S2 does not account for the dissipation of kinetic energy during deposition, the runout distance is somewhat overestimated in certain areas. The best results are obtained by S3 (Fig. 7d). In this case, there is good agreement with the measured data in terms of both the inundation area and thickness distribution of the final deposit. The simulated deposits in the source
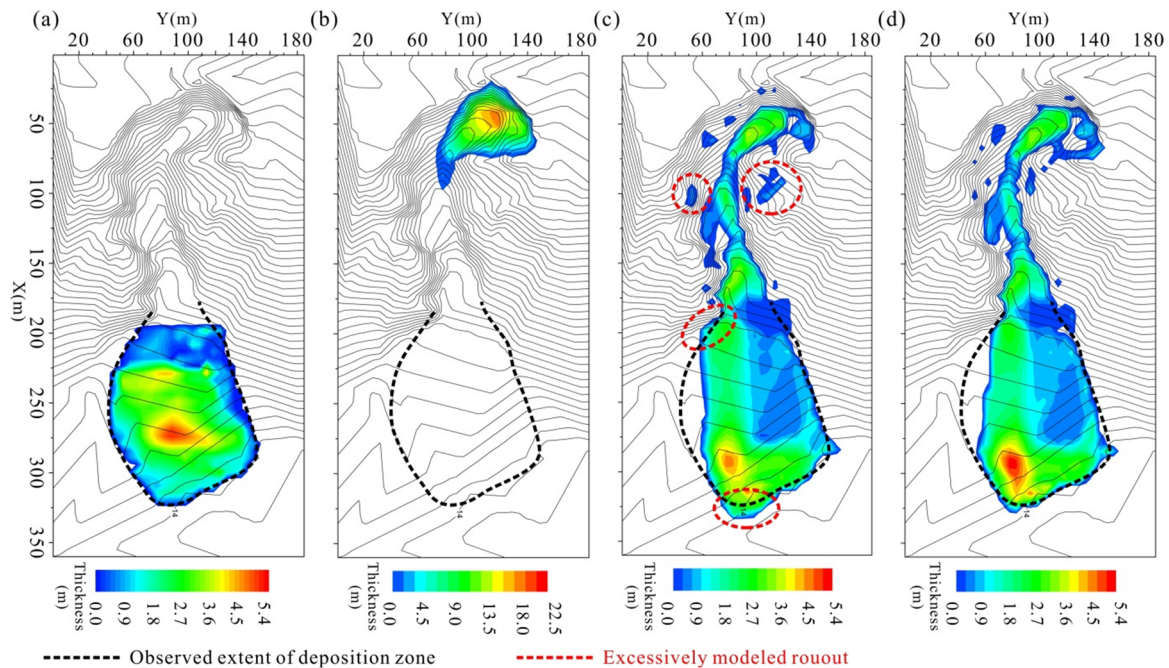

Fig. 7 Measured deposit thickness in accumulation zone and simulated final deposits in three different situations (S1: neglecting the influence of deposition, S2: without considering rheology transition and volume reduction, and S3: considering deposition and rheology transition). a) measured deposit thickness; b) case S1; c) case S2; d) case S3.

and transition zones are relatively thin with an average thickness of approximately 1 - 2 m, while the average thickness in the deposition zone is approximately 3 - 5 m. The thickness distributions in S2 and S3 are very similar. However, in S2, the landslide has a larger debris inundation area and runout distance, and the thickness of the final deposit in the deposition zone in S2 is slightly smaller than that in S3.

The above results demonstrate the good performance of the model. However, they also illustrate some discrepancies between the simulated and observed landslide thickness distributions (Fig. 7d). For instance, the observed lateral spreading of the landslide on the right hand side of the flow direction is larger than the simulation result, while the frontal thickness of the deposit is thinner than the simulated value. These errors may be caused by many factors. Here, neglecting the actual resistant influence from the damaged houses and the discrepancy between the rheology model and the actual flow rheology may be the two main reasons for these errors. These topics remain a challenge for landslide modeling and are beyond the scope of this paper, but further research needs to be done in the future.

Fig. 8 shows the simulated average velocity curves of the three cases. The simulated average velocity of S1 is the lowest, while the results of S2 and S3 are relatively close. The peak average velocity of S1 is only 0.81 m/s, while the peak average velocities of S2 and S3 are much larger (both are ~8.9 m/s), suggesting that bed deposition can significantly promote the mobility of the Gaolou landslide. On the other hand, the simulated average velocity of S2 is slightly larger than that of S3 in the first few seconds. This shows the existence of kinematic energy consumption during the rheology transition process. Additionally, there are some minor fluctuations on the average velocity curve in S2 at approximately 7.0 s, and these fluctuations are probably caused by the complex topography in the channel (e.g., some relatively abrupt changes in the slope gradient in the gully).

The simulated volume reduction curve of the landslide in S3 is shown in Fig. 9. It shows that the total volume of the landslide decreases gradually from approximately 25,300 m³ to 24,600 m³ during the propagation process, so about 700 m³ of saturated loess deposits along the traveling path. Although the volume reduction due to bed deposition is not obvious
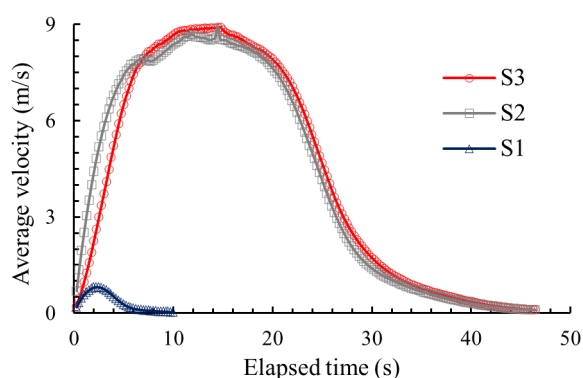

Fig. 8 Simulated average velocity curves of three situations (S1: neglecting the influence of deposition, S2: without considering rheology transition and volume reduction, and S3: considering deposition and rheology transition).
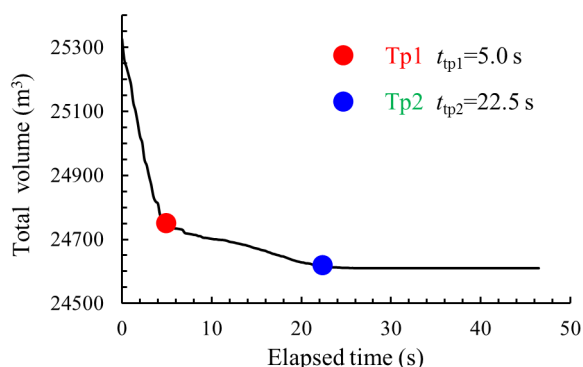

Fig. 9 Simulated reduction process of the total volume of the Gaolou landslide in S3 due to deposition. Tp1 and Tp2 represent two turning points for the movement of the landslide.

in this landslide, this small amount of deposited mass greatly influences the mobility of this landslide, as shown in the above analysis. Additionally, two inflection points exist on the volume reduction curve. The first turning point occurs at $t = 5.0$ s when the landslide has transformed into a rapid flow-like landslide, while the second turning point appears at $t = 22.5$ s when most sliding mass rests in the deposition zone and the bed deposition process stops.

The influence of rheology transition is further investigated by comparing the simulated propagation processes of this landslide in groups S2 and S3. The simulated sliding mass distributions of S2 and S3 at $t = 5.0$ s and 22.5 s are shown in Fig. 10. At $t = 5.0$ s, a larger fraction of the sliding mass enters the gully when the rheology transition is not considered (S2). Similarly, at $t = 22.5$ s, more sliding mass reaches the deposition zone in S2. This result suggests that the simulated propagation process of the landslide will be
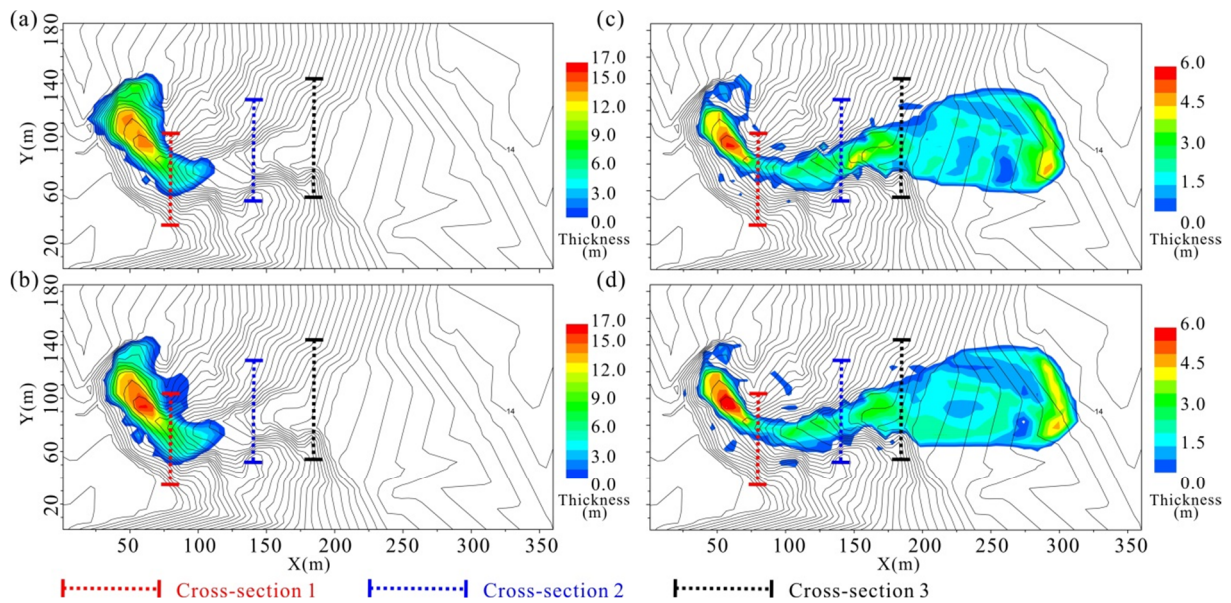
Fig. 10 Comparison of the simulated sliding mass distributions between S2 and S3 at two times (S2: without considering the rheology transition, and S3: considering deposition and rheology transition). (a) and (b) correspond to S3 and S2 at t = 5.0 s, respectively, and (c) and (d) correspond to S3 and S2 at t = 22.5 s, respectively.

faster than the real one if the energy dissipation caused by bed deposition is not considered.

Fig. 11 shows the simulated discharges in S2 and S3 at three cross-sections along the gully. These three cross-sections are located at x = 80 m, 140 m, and 180 m, representing the up, middle, and down streams of the gully, respectively. Both S2 and S3 show the same tendency where the peak discharge decreases from upstream to downstream. However, the simulated peak discharge in S2 is larger than that in S3, and the arrival time of the landslide at each cross-section in S2 is earlier than that in S3.

6 Discussion

6.1 Influence of rheological parameters on runout characteristics

The simulation results in this study depend on the calibration of the rheological parameters. In our case, the pore pressure coefficient r_u and effective cohesion c' of the sliding mass are the two main parameters determining the dynamics of a landslide. Therefore, a parametric analysis of these two parameters is conducted to check their influences on the simulation results. Two groups of simulations are analyzed. In the first group, the value of c' remains constant at 6.0 kPa when studying the influences of r_u, while the value of r_u is kept at 0.95 when checking the
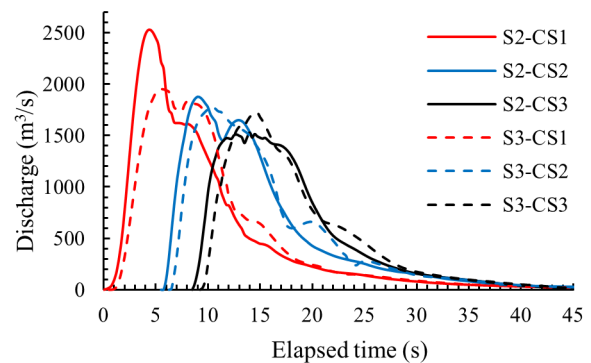

Fig. 11 Simulated discharges of the Gaolou landslide in S2 and S3 at three cross-sections (S2: without considering the rheology transition, and S3: considering deposition and rheology transition).

impact of c'. Simultaneously, all other rheological parameters have the same values as those adopted in S3. The value of r_u ranges between 0 and 1. A value of r_u = 0 means that no pore pressure will be generated, while r_u = 1 refers to the situation that is fully liquefied. Four r_u values (r_u = 0.30, 0.50, 0.70 and 0.95) which represent different levels of pore pressure extents, and three c' values (c' = 4.0 kPa, 6.0 kPa, and 8.0 kPa) are considered in this parametric study. In the second group, the simulation results of different combinations of r_u and c', which may lead to a similar inundation area close to the observed result are compared and analyzed.

Fig. 12 illustrates the influences of these two parameters on the final thickness distribution of the
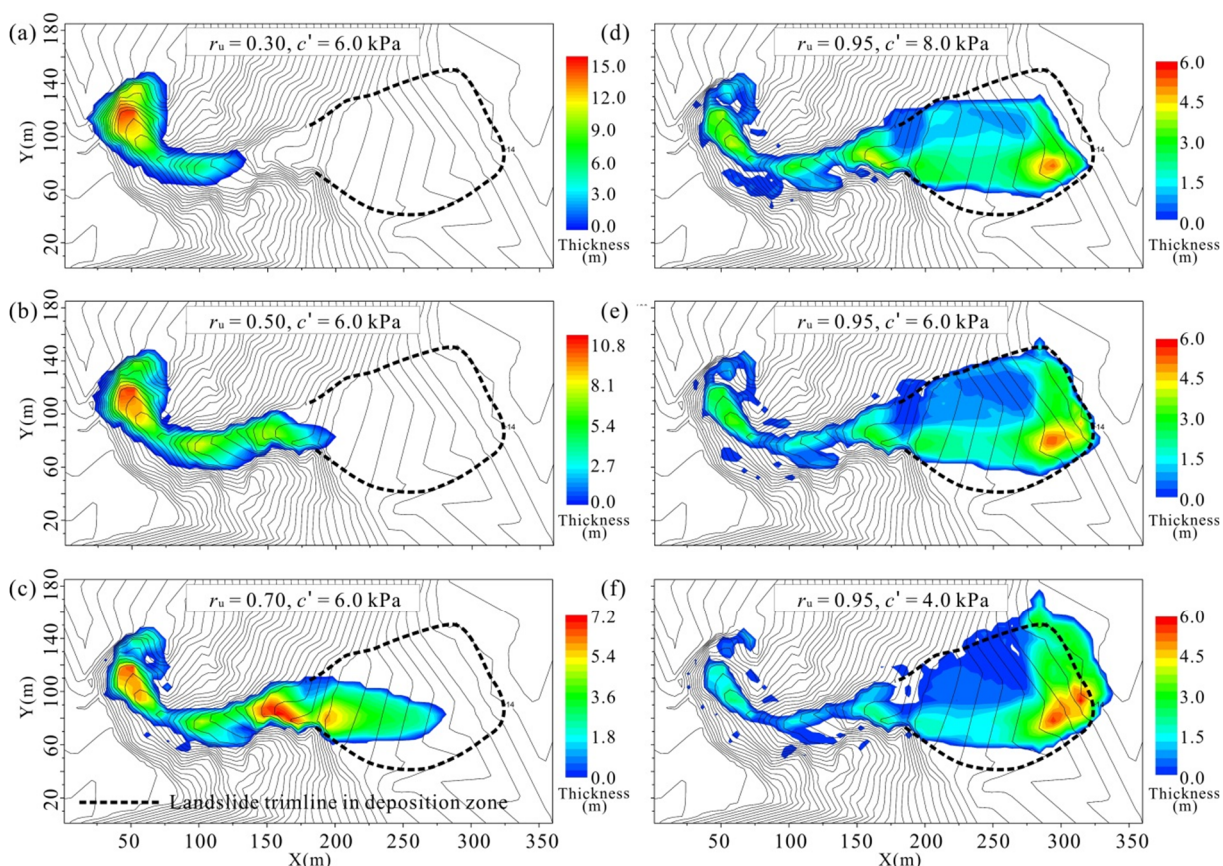
Fig. 12 Simulated final deposits with different pore pressure coefficient (r_u) and cohesion values (c').

Gaolou landslide. This shows that the runout distance of the landslide increases with an increase in the r_u value and a decrease in the c' value. The runout distance of the landslide will be significantly smaller than the actual distance when the r_u value is small (Fig. 12a-c). The result of $r_u = 0.95$ fits best with the measured landslide runout, indicating that the actual extent of basal pore pressure of this landslide should be very close to liquefaction to produce such a long runout movement. Similarly, the simulation results show that the final thickness distribution and flooded area are also sensitive to the c' value. The c' value should neither be too large nor too small. Otherwise, the flooded area will be overestimated (Fig. 12f) or underestimated (Fig. 12d). The volume of flow that reaches the deposition zone and the inundated area strongly increases when the c' value decreases. The influences of these two parameters on the average velocity of the landslide (Fig. 13) also show a similar tendency. An increase in r_u or a decrease in c' will lead to a higher flow velocity.

The simulated final deposits in the second group are illustrated in Fig. 14. This shows that we can

obtain similar simulation runout distances and inundation areas with different combinations of r_u and c' values. However, although the simulation results of all these combinations fit well with the observed results in terms of inundation area and runout distance, the thickness distribution characteristics of these combinations are evidently different. The general tendency is that more mass of
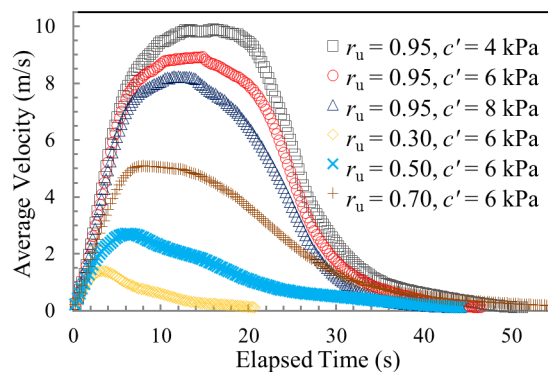

Fig. 13 Simulated average velocity curves of the landslide with different pore pressure coefficient (r_u) and cohesion values (c').
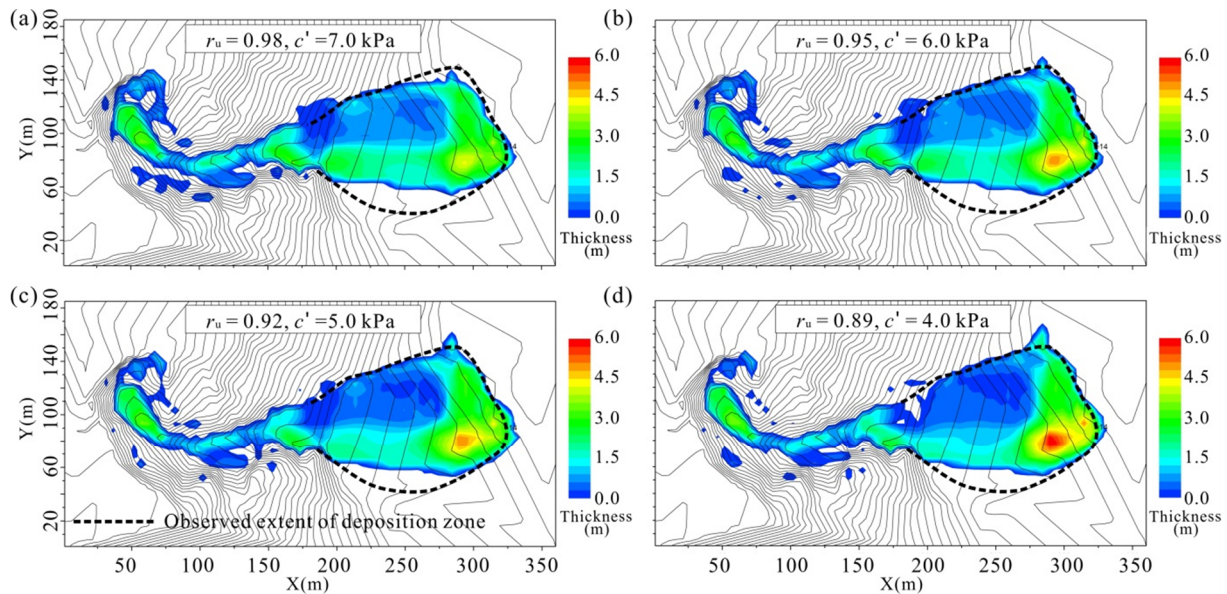
Fig. 14 Simulated final deposits with different combinations of pore pressure coefficient (r_u) and cohesion values (c') leading to similar inundation area and runout distance.

the debris will deposit at the head of the deposit when the flow is more frictional (with lower r_u value) and less plastic (with lower c' value). In comparison with other combinations, the results of $r_u = 0.95$ and $c' = 6.0$ kPa are in good agreement with the observed thickness distribution.

6.2 Impact factors of the bed deposition model

As illustrated by Eq. (6), the bed deposition rate D is related to the strength of the bed material (τ_b), shear stress at the bottom of the sliding mass (τ_s), density ρ_s, and velocity v of the sliding material. D is inversely proportional to ρ_s and v. This is because the sliding mass, which has a higher density and velocity, needs to acquire more resistance to overcome its inertia. However, the relationships among D, τ_b, and τ_s are more complex, since τ_b and τ_s are determined by many factors. Taking the Mohr-Coulomb criterion we adopted in this study as an example, τ_b and τ_s are not only related to the rheological parameters (i.e., pore pressure coefficient r_u, effective cohesion c', and the effective frictional angle φ'), but also the normal stress on the sliding surface. Additionally, the normal stress on the sliding surface is implicitly influenced by the thickness of the sliding mass, dip angle of the sliding surface, and local curvature (or the centrifugal or centripetal effects caused by irregular topography). These topics are still very challenging, and they are beyond the scope of the current study. However, they should be of interest to our future work, and more detailed field data on bed deposition could be useful for further validation of this bed deposition model.

7 Conclusion

A new depth-averaged model considering bed deposition is proposed in this paper. This model is used to simulate the Gaolou landslide and to investigate the role of bed deposition in the propagation process of this landslide. The simulation results are analyzed and discussed, and the following conclusions can be obtained.

(1) Bed deposition plays an important role in determining the hypermobility of the Gaolou landslide. During the deposition process, a thin layer of saturated soil deposits on the dry bed. The sliding surface thus shifts from the dry bed to the saturated sliding mass, promoting rapid flow-like motion of this landslide. The new model can properly depict this process, and it shows good accuracy in simulating the Gaolou landslide.

(2) Bed deposition has two major influences on the propagation of the Gaolou landslide, and both of them should be considered in the numerical simulation. First, the rheology transition associated with bed deposition will dissipate part of the kinematic energy. Therefore, the simulated runout distance and discharge tend to be overestimated if

this rheology transition is not considered. On the other hand, the thin saturated layer formed by bed deposition increases the pore water pressure on the bed, and thus enhances the motion of this landslide. If the formation of this thin layer and the impact on the rheological property of this landslide are not considered, the simulated runout distance and flooded area may be significantly underestimated.

(3) The simulation accuracy of the model presented here relies on the choice of the rheological model. It can be further improved by incorporating more sophisticated rheological and constitutive laws in the future. Additionally, the bed deposition model adopted in this study is determined by many factors. More detailed field data on bed deposition could be useful for further validation of this model in the future.

Acknowledgement

References

Alonso E, Zervos A, Pinyol N (2016) Thermo-poro-mechanical analysis of landslides: from creeping behaviour to catastrophic failure. Géotechnique 66(3): 202-219. https://doi.org/10.1680/jgeot.15.LM.006

Campbell CS (1989) Self-lubrication for long runout landslides. J Geol 97(6): 653-665. https://doi.org/10.1086/629350

Cao Z, Pender G, Wallis S, et al. (2004) Computational dam-break hydraulics over erodible sediment bed. J Hydrol Eng 130(7): 689-703. https://doi.org/10.1061/(ASCE)0733-9429(2004)130:7(689)

Chen HX, Zhang LM (2015) EDDA 1.0: integrated simulation of debris flow erosion, deposition and property changes. Geosci Model Dev 8(3): 829-844. https://doi.org/10.5194/gmd-8-829-2015

Chen X, Cui P, You Y, et al. (2015) Engineering measures for debris flow hazard mitigation in the Wenchuan earthquake area. Eng Geol 194: 73-85. https://doi.org/10.1016/j.enggeo.2014.10.002

Croissant T, Lague D, Davy P, et al. (2017) A precipiton-based approach to model hydro-sedimentary hazards induced by large sediment supplies in alluvial fans. Earth Surf Process Landf 42(13): 2054-2067. https://doi.org/10.1002/esp.4171

Crosta G, Imposimato S, Roddeman D (2009) Numerical modelling of entrainment/deposition in rock and debris-avalanches. Eng Geol 109(1-2): 135-145. https://doi.org/10.1016/j.enggeo.2008.10.004

Cuomo S, Pastor M, Capobianco V, et al. (2016) Modelling the space–time evolution of bed entrainment for flow-like landslides. Eng Geol 212: 10-20. https://doi.org/10.1016/j.enggeo.2016.07.011

Davies TR, McSaveney MJ (2009) The role of rock fragmentation in the motion of large landslides. Eng Geol 109(1): 67-79. https://doi.org/10.1016/j.enggeo.2008.11.004

Evans SG, Tutubalina OV, Drobyshev VN, et al. (2009) Catastrophic detachment and high-velocity long-runout flow of Kolka Glacier, Caucasus Mountains, Russia in 2002. Geomorphology 105(3-4): 314-321. https://doi.org/10.1016/j.geomorph.2008.10.008

Fraccarollo L, Capart H (2002) Riemann wave description of erosional dam-break flows. J Fluid Mech 461: 183-228. https://doi.org/10.1017/S0022112002008455

Goren L, Aharonov E (2007) Long runout landslides: The role of frictional heating and hydraulic diffusivity. Geophys Res Lett 34(7): L07301. https://doi.org/10.1029/2006GL028895

Haque U, Blum P, Da Silva PF, et al. (2016) Fatal landslides in Europe. Landslides 13(6): 1545-1554. https://doi.org/10.1007/s10346-016-0689-3

Heyman J, Bohorquez P, Ancey C (2016) Entrainment, motion, and deposition of coarse particles transported by water over a sloping mobile bed. J Geophys Res Earth Surf 121(10): 1931-1952. https://doi.org/10.1002/2015JF003672

Huang RQ, Pei XJ, Fan XM, et al. (2012) The characteristics and failure mechanism of the largest landslide triggered by the Wenchuan earthquake, May 12, 2008, China. Landslides 9(1): 131-142. https://doi.org/10.1007/s10346-011-0276-6

Hungr O, Evans SG (2004) Entrainment of debris in rock avalanches: an analysis of a long run-out mechanism. Geol Soc Am Bull 116(9-10): 1240-1252. https://doi.org/10.1130/B25362.1

Hungr O, Leroueil S, Picarelli L (2014) The Varnes classification of landslide types, an update. Landslides 11(2): 167-194. https://doi.org/10.1007/s10346-013-0436-y

Iverson RM (2012) Elementary theory of bed-sediment entrainment by debris flows and avalanches. J Geophys Res Earth Surf 117(F3): F03006. https://doi.org/10.1029/2011JF002189

Iverson RM, Ouyang CJ (2015) Entrainment of bed material by Earth-surface mass flows: Review and reformulation of depth-integrated theory. Rev Geophys 53(1): 27-58. https://doi.org/10.1002/2013RG000447

Johnson CG, Kokelaar BP, Iverson RM, et al. (2012) Grain-size segregation and levee formation in geophysical mass flows. J Geophys Res Earth Surf 117(F1): F01032. https://doi.org/10.1029/2011JF002185

Kang C, Chan D (2018) A progressive entrainment runout model for debris flow analysis and its application. Geomorphology 323: 25-40. https://doi.org/10.1016/j.geomorph.2018.09.003

Kang C, Chan D, Su FH, et al. (2017) Runout and entrainment analysis of an extremely large rock avalanche—a case study of Yigong, Tibet, China. Landslides 14(1): 123-139.

https://doi.org/10.1007/s10346-016-0677-7

Li TL, Zhao JF, Li P, et al. (2013) Failure and motion mechanisms of a rapid loess flowslide triggered by irrigation in the Guanzhong irrigation area, Shaanxi, China. In: Wang FW, Miyajima M, Li TL, et al. (eds.), Progress of Geo-Disaster Mitigation Technology in Asia. Springer, Berlin, Heidelberg, pp 421-433.

Liu K-F, Huang MC (2006) Numerical simulation of debris flow with application on hazard area mapping. Computat Geosci 10(2): 221-240.
https://doi.org/10.1007/s10596-005-9020-4

Liu W, He S (2020) Comprehensive modelling of runoff-generated debris flow from formation to propagation in a catchment. Landslides 17(7): 1529-1544.
https://doi.org/10.1007/s10346-020-01383-w

Liu W, He S, He Z (2019) Simulation of landslide run-out by considering frictional heating and thermal pressurization. J Mt Sci 16(1): 122-137.
https://doi.org/10.1007/s11629-018-5012-4

Mangeney A (2011) Landslide boost from entrainment. Nat Geosci 4(2): 77-78.
https://doi.org/10.1038/ngeo1077

McDougall S, Hungr O (2005) Dynamic modelling of entrainment in rapid landslides. Can Geotech J 42(5): 1437-1448.
https://doi.org/10.1139/t05-064

Medina V, Hürlimann M, Bateman A (2008) Application of FLATModel, a 2D finite volume code, to debris flows in the northeastern part of the Iberian Peninsula. Landslides 5(1): 127-142.
https://doi.org/10.1007/s10346-007-0102-3

Mergili M, Frank B, Fischer JT, et al. (2018) Computational experiments on the 1962 and 1970 landslide events at Huascarán (Peru) with r. avaflow: Lessons learned for predictive mass flow simulations. Geomorphology 322: 15-28.
https://doi.org/10.1016/j.geomorph.2018.08.032

Okada Y, Sassa K, Fukuoka H (2005) Undrained shear behaviour of sands subjected to large shear displacement and estimation of excess pore-pressure generation from drained ring shear tests. Can Geotech J 42(3): 787-803.
https://doi.org/10.1139/t05-017

Ouyang C, He S, Tang C (2015) Numerical analysis of dynamics of debris flow over erodible beds in Wenchuan earthquake-induced area. Eng Geol 194: 62-72.
https://doi.org/10.1016/j.enggeo.2014.07.012

Ouyang C, He S, Xu Q, et al. (2013) A MacCormack-TVD finite difference method to simulate the mass flow in mountainous terrain with variable computational domain. Comput Geosci 52: 1-10.
https://doi.org/10.1016/j.cageo.2012.08.024

Ouyang C, Zhao W, He S, et al. (2017) Numerical modeling and dynamic analysis of the 2017 Xinmo landslide in Maoxian County, China. J Mt Sci 14(9): 1701-1711.
https://doi.org/10.1007/s11629-017-4613-7

Pastor M, Haddad B, Sorbino G, et al. (2009) A depth-integrated, coupled SPH model for flow-like landslides and related phenomena. Int J Numer Anal Methods Geomech 33(2): 143-172.
https://doi.org/10.1002/nag.705

Perinotto H, Schneider JL, Bachèlery P, Le Bourdonnec FX, Famin V, Michon L (2015) The extreme mobility of debris avalanches: A new model of transport mechanism. J Geophys Res Solid Earth 120(12): 8110-8119.
https://doi.org/10.1002/2015JB011994

Pierson TC, Janda RJ, Thouret JC, et al. (1990) Perturbation and melting of snow and ice by the 13 November 1985 eruption of Nevado del Ruiz, Colombia, and consequent mobilization, flow and deposition of lahars. J Volcanol Geoth Res 41(1-4): 17-66.
https://doi.org/10.1016/0377-0273(90)90082-Q

Pirulli M, Pastor M (2012) Numerical study on the entrainment of bed material into rapid landslides. Géotechnique 62(11): 959-972.
https://doi.org/10.1680/geot.10.P.074

Pudasaini SP (2012) A general two-phase debris flow model. J Geophys Res Earth Surf 117(F3): F03010.
https://doi.org/10.1029/2011JF002186

Pudasaini SP, Fischer JT (2016) A mechanical erosion model for two-phase mass flows. arXiv preprint arXiv:161001806.
https://arxiv.org/abs/1610.01806v1

Sassa K, He B, Dang K, et al. (2014) Plenary: progress in landslide dynamics. In: Sassa K, Canuti P, Yin Y (eds) Landslide science for a safer geoenvironment. Springer, Cham, pp 37-67.

Shen W, Li T, Li P, et al. (2019a) A two-layer numerical model for simulating the frontal plowing phenomenon of flow-like landslides. Eng Geol 259: 105168.
https://doi.org/10.1016/j.enggeo.2019.105168

Shen W, Li T, Li P, et al. (2018) A modified finite difference model for the modeling of flowslides. Landslides 15(8): 1577-1593.
https://doi.org/10.1007/s10346-018-0980-6

Shen W, Li T, Li P, et al. (2019b) The influence of the bed entrainment-induced rheology and topography changes on the propagation of flow-like landslides: a numerical investigation. Bull Eng Geol Environ 78(7): 4771-4785.
https://doi.org/10.1007/s10064-018-01447-1

Tsou CY, Feng ZY, Chigira M (2011) Catastrophic landslide induced by typhoon Morakot, Shiaolin, Taiwan. Geomorphology 127(3-4): 166-178.
https://doi.org/10.1016/j.geomorph.2010.12.013

Wang G, Huang R, Chigira M, et al. (2013) Landslide amplification by liquefaction of runout-path material after the 2008 Wenchuan (M 8·0) earthquake, China. Earth Surf Process Landf 38(3): 265-274.
https://doi.org/10.1002/esp.3277

Wang YF, Dong JJ, Cheng QG (2017) Velocity-dependent frictional weakening of large rock avalanche basal facies: Implications for rock avalanche hypermobility? J Geophys Res Solid Earth 122(3): 1648-1676.
https://doi.org/10.1002/2016JB013624

Xu L, Dai FC, Gong QM, et al. (2012) Irrigation-induced loess flow failure in Heifangtai Platform, north-west China. Environ Earth Sci 66(6): 1707-1713.
https://doi.org/10.1007/s12665-011-0950-y

Zhang DX, Wang GH, Luo CY, et al. (2009) A rapid loess flowslide triggered by irrigation in China. Landslides 6(1): 55-60.
https://doi.org/10.1007/s10346-008-0135-2